Received: 13 February 2025 | Accepted: 7 April 2025

DOI: 10.1111/mice.13488

RESEARCH ARTICLE

COMPUTER-AIDED CIVIL AND INFRASTRUCTURE ENGINEERING WILEY

A hybrid machine learning framework for wind pressure prediction on buildings with constrained sensor networks

Foad Mohajeri Nav | **Seyedeh Fatemeh Mirfakhar** | **Reda Snaiki**

Department of Construction Engineering, École de Technologie Supérieure, Université du Québec, Montréal, Québec, Canada

Correspondence
Reda Snaiki, Department of Construction Engineering, École de technologie supérieure, Université du Québec, 1100, rue Notre-Dame Ouest, bureau A-1490, Montréal, Québec H3C 1K, Canada.
Email: reda.snaiki@etsmtl.ca

Funding information
Natural Sciences and Engineering Research Council of Canada, Grant/Award Number: CRSNG RGPIN 2022-03492

Abstract

Accurate and efficient prediction of wind pressure distributions on high-rise building façades is crucial for mitigating structural risks in urban environments. Conventional approaches rely on extensive sensor networks, often hindered by cost, accessibility, and architectural limitations. This study proposes a novel hybrid machine learning (ML) framework that reconstructs high-fidelity wind pressure (HFWP) coefficient fields from a limited number of sensors by leveraging dynamic spatiotemporal feature extraction and mapping. The methodology consists of four key stages: (1) low-fidelity pressure field reconstruction from limited sensor data using constrained QR decomposition, (2) dimensionality reduction of both low-fidelity wind pressure and HFWP reconstructions to extract dominant spatiotemporal features, (3) dynamic mapping of the reduced-order representations using a long short-term memory network, and (4) prediction of the high-fidelity pressure field reconstruction over time. The proposed approach, which predicts the time history of high-fidelity pressure coefficients for various wind directions, is validated using wind tunnel data, with case studies on multiple façades—including the windward, right-side, and leeward surfaces—under various constrained sensor placement scenarios. The proposed methodology is also evaluated against alternative ML models, demonstrating superior accuracy in reconstructing the full pressure field. The results highlight the robustness and generalization capability of the model across different wind directions and sensor configurations, making it a practical solution for real-time wind pressure estimation in structural health monitoring and digital twin applications.

1 | INTRODUCTION

High-rise buildings, with their distinctive geometric forms and exposure to turbulent wind flows, are particularly susceptible to wind-induced effects (Hou & Jafari, 2020). The stochastic nature of wind flow, coupled with the complex interplay between the structure's form and the surrounding urban environment (Pezeshki et al., 2024), results in intricate pressure distributions across the building envelope (Avini et al., 2019; Han et al., 2022). Various solutions, such as vibration control strategies, have been developed, aiming to design resilient and robust structures (Kim &

Adeli, 2005; Pezeshki et al., 2023; Wang & Adeli, 2015). To achieve this, accurately predicting wind pressure distributions is essential, as it helps optimize façade performance (Luo & Kareem, 2021; McGuill & Keenahan, 2020), mitigate risks of structural damage (Montazeri & Blocken, 2013), and ensure the serviceability of buildings (Avini et al., 2019). Four primary approaches have been developed to predict wind-induced pressures on building façades, each offering unique strengths and limitations: computational fluid dynamics (CFD), wind tunnel testing, field measurements, and data-driven techniques.

CFD has become a valuable tool for simulating wind pressures on high-rise buildings (Aboshosha et al., 2015; Bre & Gimenez, 2022; Dogan & Kastner, 2021; Meng et al., 2018; Montazeri & Blocken, 2013). By solving the governing equations of fluid flow using models such as Reynolds-averaged Navier–Stokes or large eddy simulations, CFD enables detailed exploration of wind flow around structures with complex geometries (Arbelo Romero et al., 2024). This approach provides valuable insights into the spatial and temporal variations of wind pressures, facilitating parametric studies (McGuill & Keenahan, 2020) and aiding in the design of aerodynamic structures (Kociecki & Adeli, 2014; Sharma et al., 2018). Despite these advantages, CFD remains computationally expensive, requiring significant computational resources and expertise in model setup, mesh generation, and turbulence modeling (Ahmadi et al., 2022; Amini & Memari, 2021; Tominaga et al., 2023). Furthermore, the accuracy of CFD simulations is highly sensitive to the chosen turbulence model, the quality of the computational mesh, and the appropriate representation of boundary conditions, particularly in complex urban environments (Tominaga et al., 2023).

Wind tunnel testing, a well-established experimental technique in wind engineering, complements CFD by offering reliable physical data (Al Sayegh et al., 2025; Zhao et al., 2024). Scaled models of high-rise buildings subjected to controlled wind conditions in specialized facilities allow researchers to directly measure aerodynamic forces and pressures (Liang et al., 2020). Wind tunnel tests are pivotal for studying phenomena such as vortex shedding, buffeting, and flow separation, and they serve as benchmarks for validating numerical simulations. However, the labor-intensive and resource-demanding nature of wind tunnel tests, coupled with scaling challenges, limits their applicability for iterative design processes or large-scale investigations (Han et al., 2022; Whiteman et al., 2022).

Field measurements bridge the gap between experimental and real-world conditions by capturing wind-induced pressures directly from actual structures (Hochschild & Gorlé, 2024a, 2024b). Pressure sensors installed on building façades and roofs provide dynamic, site-specific data, accounting for local topography, urban roughness, and other environmental factors (Gao et al., 2023; Luo et al., 2023). These measurements are crucial for validating numerical models, refining building codes, and improving the predictive capabilities of wind tunnel and CFD studies (Inoba et al., 2022). However, deploying extensive sensor networks is costly, and physical constraints such as accessibility and aesthetic considerations often result in suboptimal sensor configurations (Luo et al., 2023). Furthermore, the spatial and temporal resolution of field measurements may be insufficient to capture the full spectrum of wind-induced pressure fluctuations (Han et al., 2022).

Data-driven machine learning (ML) techniques have gained significant traction in wind engineering, offering promising alternatives to conventional methods (Lamberti & Gorlé, 2021; Wu & Snaiki, 2022). A wide range of applications has been explored, including those related to wind and aerodynamic phenomena (e.g., Cid Montoya et al., 2024; Clemente et al., 2024; Entezami & Sarmadi, 2024; Gu et al., 2025; Li et al., 2021a; Nav & Snaiki, 2025; Oh et al., 2019) and others addressing structural performance and control (Azimi & Yang, 2024; Inoue et al., 2023; Li et al., 2021b; Yao et al., 2024). By training ML algorithms on large datasets generated from CFD simulations, wind tunnel tests, and field measurements, it is possible to develop predictive models that can rapidly and accurately estimate wind pressures on building façades (Fernández-Cabán et al., 2018; Huang et al., 2022; Li et al., 2022). Various ML models, including clustering algorithms (Kim et al., 2021), gradient boosting decision trees (Hu & Kwok, 2020; Weng & Paal, 2022), and artificial neural networks (ANNs; Bre et al., 2018), have been employed to estimate wind pressures on buildings. More advanced models, such as generative adversarial networks (Hu et al., 2019), extreme gradient boosting, and deep neural network models (Huang et al., 2022; Meddage et al., 2024, 2025), leverage high-density experimental or simulated data for improved accuracy. These models can potentially capture complex non-linear relationships between wind characteristics, building geometry, and pressure distributions that may be difficult to represent using conventional analytical or numerical methods. However, the success of data-driven approaches hinges on the availability of high-quality, diverse datasets, the appropriate selection and training of ML algorithms, and the ability to generalize the learned models to new and unseen scenarios (Gao et al., 2023; Snaiki & Mirfakhar, 2024). Many current techniques rely on dense sensor networks and focus on mean or peak pressure predictions, often neglecting transient aerodynamic effects (Meddage et al., 2024; Wei et al., 2025). Furthermore, reconstructions based on a single wind direction may not generalize to other wind conditions (Snaiki & Mirfakhar, 2024).

Central to many of the discussed approaches, particularly field measurements, wind tunnel tests, and data-driven techniques, is the effective utilization of sensor data (Gao et al., 2024; Hochschild & Gorlé, 2024a). Accurate and reliable measurements of wind pressures on building surfaces are crucial for validating numerical simulations, calibrating empirical models, and providing valuable insights into real-world wind-building interactions (Huang et al., 2022; Li et al., 2024). However, deploying and maintaining extensive sensor networks on high-rise buildings can be challenging due to logistical constraints, environmental interference, and high implementation costs (Amezquita-Sanchez et al., 2018; Luo et al., 2023). Practical constraints such as limited accessibility, aesthetic considerations, and the cost of installation and maintenance often necessitate using parse sensor arrays (Gao et al., 2024; Inoba et al., 2022). This raises critical questions regarding the optimal placement of sensors to maximize information capture while minimizing the number of sensors required (Karnik et al., 2024). Effective sensor placement strategies are crucial for ensuring that the collected data accurately represents the spatial and temporal variations of wind pressures across the building envelope, enabling robust model development and reliable predictions (Erichson et al., 2020; Gutierrez Soto & Adeli, 2013; Wang et al., 2025).

This study introduces a novel hybrid ML framework designed to accurately and efficiently reconstruct wind pressure distributions on high-rise building façades using data from constrained and sparse sensor networks. The methodology is structured into four main stages: (1) low-fidelity pressure field reconstruction from limited sensor data using a constrained QR decomposition with a pivoting technique (where "low-fidelity" refers to the pressure field reconstructed from sparse sensor measurements), (2) dimensionality reduction of both low-fidelity wind pressure (LFWP) and high-fidelity wind pressure (HFWP) reconstructions using proper orthogonal decomposition (POD) to extract dominant spatiotemporal features (where "high-fidelity" represents the complete pressure field), (3) surrogate model training using long short-term memory (LSTM) networks to establish a dynamic mapping between the reduced-order representations, and (4) prediction of the high-fidelity pressure field reconstruction over time from the LSTM output. The performance of the framework will be comprehensively evaluated using wind tunnel data from Tokyo Polytechnic University (TPU) across multiple façades of a high-rise building under various challenging constrained sensor placement scenarios, including predefined sensor locations, restricted sensor placement regions, and configurations with a limited number of sensors. Furthermore, the framework's performance will be compared against alternative ML models.

2 | METHODOLOGY

This study presents a novel framework for the accurate and efficient reconstruction of dynamic wind pressure distributions on building façades, specifically addressing the challenge of using data from extremely limited and constrained sensor networks. While prior methods, such as that by Snaiki and Mirfakhar (2024), demonstrate effective pressure field reconstruction, they typically require a substantial number of sensors. Attempting to apply such methods with the sparse sensor counts considered in this study (e.g., five sensors) would yield significantly degraded, low-fidelity pressure field reconstructions. The core innovation of this work lies in a dynamic mapping process designed to effectively enhance these inherently poor, low-fidelity reconstructed inputs derived from severely constrained sensor arrangements. Furthermore, unlike the work by Snaiki and Mirfakhar (2024), which primarily focused on a single wind direction, the proposed methodology is designed to handle multiple wind directions, significantly enhancing its practical applicability.

The proposed methodology consists of four main stages (visualized in Figure 1): (1) reconstructing a low-fidelity representation of the full pressure field from the sparse sensor data using constrained sensor placement techniques, (2) extracting dominant spatiotemporal dynamic features from both this low-fidelity pressure reconstruction and corresponding high-fidelity pressure reconstruction using POD (Conti et al., 2024), (3) training an LSTM network to establish a dynamic mapping between the reduced-order representations (Conti et al., 2024), and (4) reconstructing the predicted high-fidelity pressure field time history from the LSTM output. Here, high-fidelity refers to the entire pressure field reconstruction (e.g., from dense sensors or simulation), while low-fidelity refers to the initial, potentially degraded, reconstruction of the pressure field from the sparse sensors. This dynamic mapping allows the model to significantly improve the low-fidelity reconstruction and predict the time history of the high-fidelity pressure field. The subsequent sections detail the specific methodologies employed for each stage.

2.1 | Sensor placement for pressure field reconstruction

Accurately reconstructing the complete wind pressure field from limited sensor data is an essential initial step. This process aims to generate a low-fidelity reconstruction of the pressure distribution based on the limited measurements available (Step 1 of Figure 1). Strategic sensor

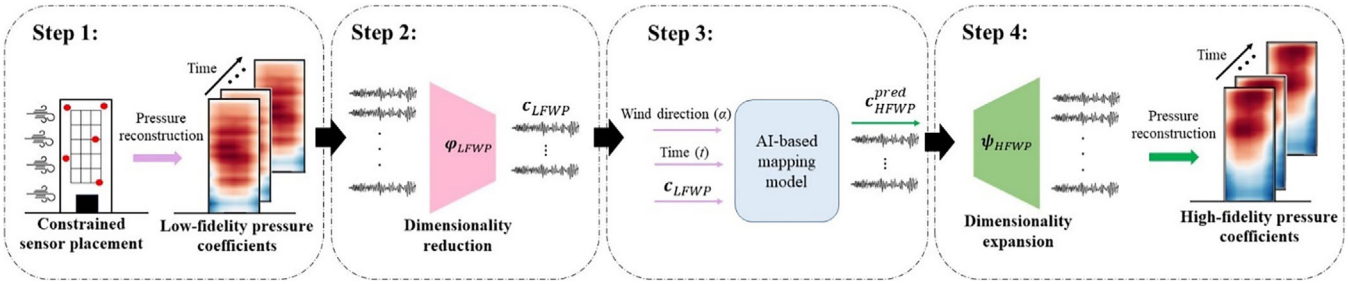

FIGURE 1 Schematic representation of the proposed framework.

placement plays a crucial role in effectively capturing the dominant dynamics of the wind pressure field.

In this study, QR decomposition with pivoting (QRDP), a well-established technique, is employed to identify optimal sensor locations. QRDP prioritizes locations based on the linear independence of their associated data, maximizing the information captured. The methodology proceeds as follows. Wind pressure data are obtained from experimental wind tunnel tests on a high-rise building. The collected data are organized into a snapshot matrix $\boldsymbol{X} \in \mathbb{R}^{m \times n}$, where m denotes the number of spatial locations and n the number of time instances. POD is then applied to extract the dominant modes of variability in the wind pressure field. This is achieved by performing singular value decomposition (SVD) on the snapshot matrix. The first r dominant spatial modes, corresponding to the largest singular values, are retained, capturing the majority of the energy in the dataset. These modes denoted as $\boldsymbol{\Phi} = [\boldsymbol{u}_1, \boldsymbol{u}_2, \ldots, \boldsymbol{u}_r]$, represent the critical regions of variability in the wind pressure field.

To identify the optimal sensor locations, QR decomposition with column pivoting is performed on the transposed matrix of the retained modes, $\boldsymbol{\Phi}^{\mathrm{T}}$. The decomposition is expressed as

$$\boldsymbol{\Phi}^{\mathrm{T}}\boldsymbol{P} = \boldsymbol{Q}\boldsymbol{R} \tag{1}$$

where $\boldsymbol{P}$ is the permutation matrix that reorders the columns of $\boldsymbol{\Phi}^{\mathrm{T}}$; $\boldsymbol{Q}$ is the orthogonal matrix; and $\boldsymbol{R}$ is the upper triangular matrix. The pivot matrix $\boldsymbol{P}$ provides the indices of the most informative locations for sensor placement by prioritizing the columns of $\boldsymbol{\Phi}^{\mathbf{T}}$ that exhibit the highest linear independence. The number of sensors is determined based on a predefined energy threshold, such as capturing a specific percentage of the total variance in the wind pressure field. The corresponding sensor locations are then selected based on the dominant pivot indices obtained from $\boldsymbol{P}$. Finally, the sensor placement is validated by reconstructing the wind pressure field using data from the selected sensor locations and comparing it with the original dataset. This methodology ensures that the chosen sensor configuration provides maximum information with minimal redundancy, enabling accurate and efficient monitoring of wind pressure on the building's surface.

While QRDP provides an ordered ranking, practical considerations such as cost, accessibility, and spatial constraints often necessitate selecting a subset of the top-ranked locations. To address these constraints, constrained optimization techniques can be integrated with QRDP, refining sensor placement while ensuring practical feasibility and maintaining the efficacy of subsequent dimensionality reduction. Several optimization frameworks have been developed in the literature (e.g., Karnik et al., 2024; Snaiki & Mirfakhar, 2024) to adapt QR decomposition techniques for constrained sensor placement. Specifically, when sensor locations are subject to constraints, the QR decomposition algorithm can be modified to ensure that the selected sensor locations satisfy the specified limitations while simultaneously optimizing data acquisition. This adaptation typically involves modifying the pivot selection strategy within the QR decomposition process (Karnik et al., 2024). Instead of solely prioritizing columns with the largest two norms, the modified algorithm prioritizes permissible indices that comply with the constraints while maintaining a high degree of linear independence among the selected columns. By restricting the pivot selection process during the final $r - s$ steps of the QR decomposition, where s denotes the number of sensors allowed in the constrained region or the total number of predetermined sensors, the method effectively preserves the most significant contributors to the objective function (Karnik et al., 2024; Snaiki & Mirfakhar, 2024). The integration of constraints within the QR pivoting procedure varies depending on the specific constraint type. Fundamentally, the algorithm prioritizes maximizing the leading diagonal entries of the upper triangular matrix $\boldsymbol{R}$ during the initial iterations, establishing strong diagonal dominance essential for numerical stability and convergence. Subsequently, domain-specific constraints are enforced in the later stages (final $r - s$ steps) to optimize the trailing sub-diagonal entries (R_{ii}). By confining the pivot selection to permissible locations that satisfy the constraints, this approach ensures

adherence to domain limitations while minimizing the impact on the previously established diagonal dominance (Karnik et al., 2024; Snaiki & Mirfakhar, 2024).

This study investigates three constrained scenarios for sensor placement: (1) the predefined sensor locations, (2) the restricted sensor placement regions, and (3) the limited number of sensors. For the first two sensors, an identical number of sensors (25 in this case) is employed. In the third scenario, only five sensors are selected, corresponding to the first five dominant modes identified through the QR decomposition technique. It is important to note that sensor placement optimization was performed differently for different building façades. For the windward façade, sensor placement optimization is performed for a wind direction perpendicular to the building façade (0°). For the right-side and leeward façades, the sensor placement optimization is performed for a wind direction of 50°. The optimal sensor locations determined for these specific wind directions are subsequently applied to all other wind directions for the corresponding façade. While this approach may not guarantee optimal results for all wind directions, it will be demonstrated that the proposed algorithm effectively addresses all constrained scenarios based on the approximated sensor locations. It is important to emphasize that the pressure coefficients obtained through this process represent a low-fidelity reconstruction of the actual pressure field. The subsequent methodology aims to enhance this low-fidelity representation to achieve a high-fidelity reconstruction of the wind pressure distribution.

2.2 | Dimensionality reduction

Dimensionality reduction is a critical pre-processing step in this methodology. Directly training a surrogate model on high-dimensional, time-dependent data (e.g., wind pressure) can be computationally prohibitive, prone to overfitting, and may hinder the model's ability to generalize. POD is employed in this study to address these challenges. POD is a powerful technique for extracting dominant spatiotemporal features from high-dimensional data. It identifies the most energetic modes of variability, effectively transforming the data into a reduced-order subspace. While other dimensionality reduction techniques exist, such as autoencoders (e.g., Naeini & Snaiki, 2024) and dynamic mode decomposition (DMD), POD was chosen due to its optimality in capturing energy content and its computational efficiency (Conti et al., 2024).

This section outlines the process for extracting the dominant spatiotemporal features from both low-fidelity and high-fidelity pressure field reconstructions using POD. Although both datasets are derived from the same wind tunnel experiments, a key distinction is made based on the sensor coverage employed in the reconstruction process. High-fidelity reconstructions of the pressure field are obtained using a nearly complete sensor network, yielding a detailed and accurate spatial representation of the wind pressure distribution. In contrast, low-fidelity reconstructions based on a limited subset of sensors produce a less detailed and lower-resolution representation of the pressure field. This difference in fidelity does not arise from the inherent accuracy of the sensor measurements but rather from the density of sensor coverage employed during the reconstruction process.

The LFWP reconstruction, denoted as $X_{LFWP} \in \mathbb{R}^{m\times n}$, where m represents the number of spatial points across the building façade and n denotes the number of time instants, is constructed from the sparse sensor network derived using the constrained sensor placement strategy described in Section 2.1 (Step 1 in Figure 1). This reconstruction, based on a limited number of sensors, yields an approximate and degraded representation of the full pressure field. In contrast, the HFWP reconstruction, denoted as $X_{HFWP} \in \mathbb{R}^{m\times n}$, is obtained directly from the complete set of pressure sensors available in the wind tunnel tests, providing a detailed and accurate pressure distribution. Both X_{LFWP} and X_{HFWP} are arranged into snapshot matrices, forming a rectangular structure in which each row corresponds to a measurement location on the building façade, and each column represents a discrete time instant. To extract the dominant spatiotemporal features, SVD is applied to each snapshot matrix as follows (Step 2 in Figure 1):

$$X_{LFWP} = U_{LFWP}\, S_{LFWP} V_{LFWP}^{T} \tag{2}$$

$$X_{HFWP} = U_{HFWP}\, S_{HFWP} V_{HFWP}^{T} \tag{3}$$

where U_{LFWP}, U_{HFWP} are the orthogonal matrices of left singular vectors (POD modes) for LFWP and HFWP, respectively; S_{LFWP}, S_{HFWP} are the diagonal matrices containing singular values (representing the energy content of each mode) for LFWP and HFWP, respectively; and V_{LFWP}, V_{HFWP} are the orthogonal matrices of right singular vectors for LFWP and HFWP, respectively. To reduce the spatial dimensionality of the pressure field, only the k most significant singular values and their corresponding left singular vectors are retained. The number of retained modes, k, is determined by capturing a desired percentage (ε) of the total variance in the data, typically expressed as

$$k = \min\left\{ k : \frac{\sum_{i=1}^{k} \sigma_i^2}{\sum_{i=1}^{N} \sigma_i^2} \geq \varepsilon \right\} \tag{4}$$

where σ_i is the ith singular value; N is the total number of singular values; and ε is the desired variance capture percentage (e.g., 0.90 for 90% variance capture). This criterion ensures that the retained modes ($U_{LFWP,k}, U_{HFWP,k}$) represent the dominant energy content of the flow field.

After identifying the k dominant POD modes for both datasets, the original data matrices X_{LFWP} and X_{HFWP} are projected onto the subspace spanned by these modes, yielding the corresponding POD coefficients c_{LFWP} and c_{HFWP}:

$$c_{LFWP} = U_{LFWP,k}^T X_{LFWP} \tag{5}$$

$$c_{HFWP} = U_{HFWP,k}^T X_{HFWP} \tag{6}$$

These coefficients capture the evolution of the dominant modes over time and serve as the input features for the surrogate model training in the subsequent section. By transforming the data into a reduced-order space that captures the dominant dynamics, POD enables the LSTM-based model to establish a robust and physically meaningful mapping from low-fidelity to high-fidelity pressure representations.

2.3 | Dynamic mapping with LSTM

Following the dimensionality reduction process, the time-dependent POD coefficients, c_{LFWP} and c_{HFWP}, which represent the dominant dynamics of the low- and high-fidelity reconstructions, respectively, are used to train a surrogate model. This approach leverages the reduced-order representation of the data, achieved through POD, to establish a mapping between the low-fidelity and high-fidelity representations. By working in this reduced-order space, the surrogate model can learn the complex dynamic relationships between the low-fidelity and high-fidelity representations more effectively, mitigating the computational burden associated with direct mapping in the original high-dimensional space.

In this study, an LSTM network is employed as the surrogate model to approximate the mapping function, f, following Conti et al. (2024). LSTM networks are a type of recurrent neural network particularly well-suited for capturing temporal dependencies in sequential data. Their ability to model the evolution of POD coefficients makes them ideal for this application. The LSTM network is trained to approximate the following functional relationship:

$$f\left(c_{LFWP}, t, \alpha\right) = c_{HFWP} \tag{7}$$

where α is the mean wind incidence angle, measured relative to the building façade's normal (hereafter referred to as wind direction); and t is time. The LSTM network is designed to learn dynamic mapping. It takes, as input, sequences of both wind direction and low-fidelity POD coefficients. Over time steps ($\tau = 1, 2, \ldots, t$), the LSTM processes these input sequences and learns to predict the corresponding sequence of high-fidelity POD coefficients (Step 3 in Figure 1). An LSTM layer consists of multiple memory cells, which serve as the fundamental units for processing sequential data. Each memory cell features a sophisticated gating mechanism to regulate information flow, comprising four key components: an internal cell state and three gates—input, forget, and output. These gates, along with the cell state, are parameterized by learnable weights and biases. Through this mechanism, the LSTM selectively updates, retains, and outputs information from the cell state, enabling it to learn and exploit long-range dependencies in sequential data.

2.4 | High-fidelity pressure field reconstruction

The final stage of the proposed framework involves reconstructing the full high-fidelity pressure field time history using the output from the trained LSTM network. Upon successful training, the LSTM model can predict the temporal evolution of the high-fidelity POD coefficients, denoted as c_{HFWP}^{pred}, based on the input low-fidelity coefficients, c_{LFWP}. These predicted coefficients are then used to reconstruct the estimated high-fidelity pressure coefficient field, X_{HFWP}^{pred}, through the following reconstruction formula:

$$X_{HFWP}^{pred} = U_{HFWP,k}\, c_{HFWP}^{pred} \tag{8}$$

This reconstruction process involves multiplying the matrix of high-fidelity POD modes by the predicted high-fidelity POD coefficients, c_{HFWP}^{pred}. This operation effectively projects the predicted dynamics from the reduced-order subspace back into the full spatial domain, thereby yielding a prediction of the HFWP field (Step 4 of Figure 1). A schematic representation of the proposed framework is presented in Figure 1.

3 | CASE STUDY

This section details the application of the proposed POD-LSTM framework for dynamic wind pressure field reconstruction on a high-rise building. To rigorously evaluate the framework's performance and practical applicability, several case studies are examined. These case studies focus on three constrained sensor placement scenarios, designed to

reflect real-world limitations in sensor deployment: (1) predefined sensor locations, (2) restricted sensor placement regions, and (3) a limited number of sensors. Furthermore, the evaluation includes predictions for multiple building façades (windward, right-side, and leeward) and a comparative analysis against alternative ML approaches. This comprehensive analysis demonstrates the framework's ability to accurately predict time-dependent pressure distributions under various practical constraints and complex flow conditions.

3.1 | Wind tunnel dataset and sensor configurations

The case study utilizes wind tunnel data from the TPU aerodynamic database, which provides HFWP coefficients for a high-rise building model subjected to various wind directions. The experimental setup consists of a scaled building model tested in a boundary-layer wind tunnel, with pressure taps distributed across its façades to capture wind-induced pressure fluctuations. The wind pressure data were generated through controlled experiments conducted in an open-circuit wind tunnel with a 1.2 by 1.0 m test section. A 1:400 scale model of the building was subjected to simulated turbulent wind flow with a power-law profile (exponent 1/4) and a peak wind speed of 11 m/s. Turbulence characteristics were calibrated to represent Category III (suburban terrain) conditions. The building model was instrumented with 500 pressure taps evenly distributed across the four façades, arranged in a 5 by 25 grid on each façade. Pressure measurements were recorded at a 1 kHz sampling rate. In this study, two levels of data fidelity are defined based on sensor coverage:

1. High-fidelity reconstruction (X_{HFWP}): Obtained directly from the full set of pressure taps available in the TPU database, representing a highly detailed and accurate distribution of wind pressure coefficients.
2. Low-fidelity reconstruction (X_{LFWP}): Constructed using a limited subset of sensors, selected based on the constrained sensor placement strategies described in Section 2.1. The pressure coefficient field reconstructed from these sparse data serves as the low-fidelity input for the dynamic mapping process.

It should be noted that the selection of an appropriate temporal window is essential for capturing key aerodynamic phenomena such as vortex shedding and flow separation. To ensure all dominant flow features are recorded, the frequency content of the pressure signals is analyzed and a window spanning multiple shedding cycles is chosen. In this study, 8000 time steps at 0.001 s each were selected, resulting in a total duration of 8 s of data.

The dataset comprises 11 wind directions (α) (Figure 2a), ranging from 0° to 50° in 5° increments. Here, 0° indicates wind that is perpendicular to the primary façade, while positive angles indicate a clockwise rotation. Owing to the building's symmetric geometry, wind directions beyond 50° exhibit similar flow characteristics. For model evaluation, eight wind directions are allocated for training, and the remaining three are reserved for testing.

In addition to the windward façade, which is often more straightforward to reconstruct due to relatively uniform pressure distributions, the study extends to the right-side and leeward façades, where complex flow interactions—such as vortex shedding and wake turbulence—pose greater challenges for wind pressure coefficient prediction. This allows for a more rigorous assessment of the framework's ability to reconstruct high-fidelity pressure distributions across different aerodynamic conditions.

The proposed hybrid methodology operates on the full wind pressure field without subtracting the mean flow, preserving both steady and fluctuating components to ensure accurate reconstruction of the complete pressure distribution. The mean flow is removed only during the QR decomposition-based sensor placement optimization to ensure that sensor locations are selected based on the dominant fluctuating features of the pressure field rather than the static mean distribution.

3.2 | Constrained sensor placement and low-fidelity reconstruction

To evaluate the proposed framework under realistic sensor deployment constraints, several constrained sensor placement scenarios are considered as outlined in Section 2.1 and shown in Figure 2. These scenarios include:

1. Predefined sensor locations: This scenario addresses situations where a subset of sensors is already installed on the building façade or where specific sensor locations are predetermined due to structural, logistical, or legacy system constraints. The remaining sensors are then optimally placed while taking into account the existing sensor configuration. This setup mimics real-world retrofitting or expansion of existing monitoring systems (Figure 2c).
2. Restricted sensor placement regions: This scenario considers situations where certain areas of the façade are inaccessible or unsuitable for sensor placement due to the presence of architectural features (e.g., windows, doors), structural elements, or other practical restrictions (Figure 2d). The sensor placement algorithm is

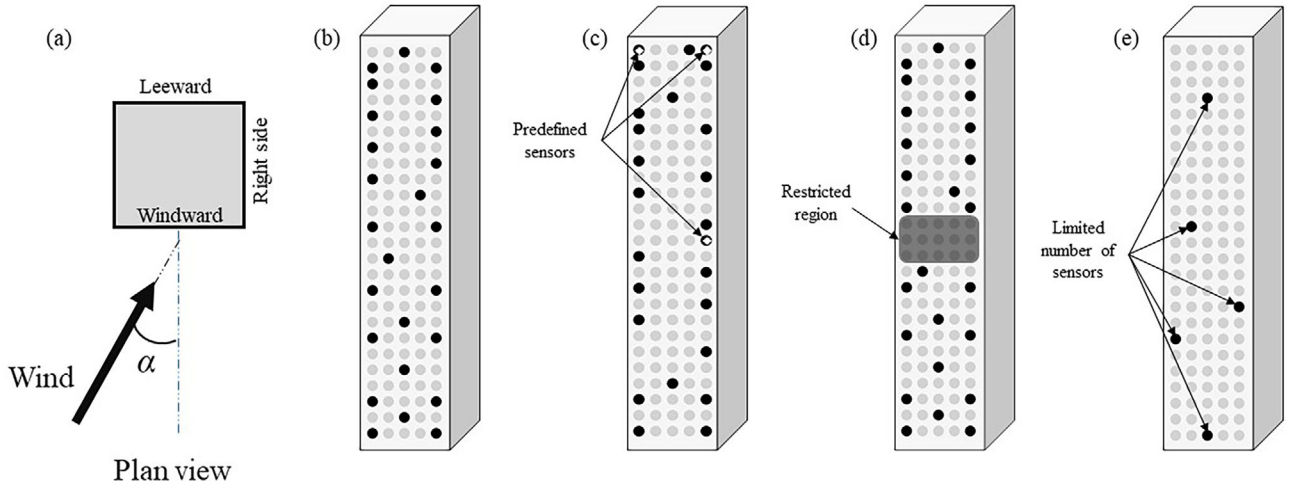

FIGURE 2 (a) Wind direction (α) in the plan view and sensor configurations for the four scenarios in the windward case: (b) unconstrained, (c) predefined locations, (d) restricted region, and (e) limited number of sensors.

constrained to avoid these designated regions, optimizing the placement of the available sensors within the permitted areas. This scenario assesses the adaptability of the proposed framework to complex façade geometries and practical limitations.

3. Severely limited number of sensors: This scenario addresses budget constraints or situations where minimizing the number of sensors is a primary objective. The framework is evaluated with a significantly reduced number of sensors (Figure 2e), pushing the limits of accurate field reconstruction. This represents a more challenging scenario, as capturing the full complexity of the pressure field with very few measurement points is inherently difficult. This evaluation determines the framework's performance under extreme resource limitations and identifies the minimum number of sensors required for acceptable accuracy.

For each sensor placement scenario, a low-fidelity pressure coefficient field is reconstructed using the constrained QRDP technique as detailed in Section 2.1. This method selects a minimal yet optimal set of sensors and utilizes their measurements to estimate the full pressure coefficient field. The resulting low-fidelity snapshot matrix X_{LFWP} is constructed, where each row represents a spatial location (125 in total), and each column corresponds to a time instant (8000 in total, with a time step of 0.001 s, covering a duration of 8 s). While this reconstruction does not fully resolve the fine-scale spatial complexity of wind-induced pressure variations, it effectively captures the dominant pressure distribution characteristics. This low-fidelity representation serves as the input for the dynamic mapping process, where the LSTM-based surrogate model enhances the initial reconstruction to predict the corresponding HFWP coefficient field. By training the LSTM model to learn the relationship between the low-fidelity and high-fidelity POD coefficients, the proposed framework effectively reconstructs the complete HFWP coefficient field, even when sensor availability is highly constrained.

3.3 | Training performance

As described in Section 2.2, the POD technique is employed to reduce the dimensionality of both the LFWP reconstructions, derived from sparse sensor measurements, and the HFWP reconstructions, representing the complete pressure field obtained using all available pressure taps during wind tunnel experiments. Following dimensionality reduction, LSTM models are trained to establish a dynamic mapping between the low-fidelity and high-fidelity representations. The LSTM models are trained for each of the following sensor placement scenarios: (1) unconstrained sensor placement, (2) predefined sensor locations, (3) restricted sensor placement region, and (4) limited number of sensors. The sensor configurations for these four scenarios are visually presented in Figure 2 for the windward case. Additionally, for the unconstrained sensor placement scenario, separate LSTM models are trained for each building façade (windward, right-side, and leeward) using 25 sensors to reconstruct the LFWP field.

To evaluate the effectiveness of LSTM training, the following analysis focuses on the windward façade for the unconstrained scenario. The same methodology is applied to all other scenarios and façades, yielding comparable results. In this scenario, 15 POD modes are retained for both the LFWP and HFWP datasets for LSTM training. The LSTM network is designed to predict the time series of HFWP POD coefficients (c_{HFWP}) using time, wind

direction, and LFWP POD coefficients (c_{LFWP}) as inputs. This results in an LSTM model with 17 input features and 15 output features.

The hyperparameter optimization of the LSTM network, including learning rate, batch size, and network architecture, was conducted using Bayesian optimization. The Bayesian optimization process iteratively evaluates 100 different trials, minimizing the loss function to identify the best hyperparameter combination. The following key parameters were explored:

1. Hidden dimension: Ranges between 32 and 1024.
2. Number of LSTM layers: Ranges between 1 and 8.
3. Learning rate: Varies between 1e-6 and 1e-2 on a logarithmic scale.
4. Batch size: Ranges between 16 and 512.

During each trial, the model is trained for 200 epochs, and the validation loss is used to guide the search for better hyperparameters. The Adam optimizer is employed for training, and mean squared error (MSE) is used as the loss function to assess model performance. Once the optimal hyperparameters are identified, the final model is trained for 2000 epochs using the selected settings and saved for further testing. Additionally, early stopping is employed to prevent overfitting, and dropout regularization is integrated into the LSTM layers to further reduce overfitting risks. This Bayesian optimization approach effectively balances exploration and exploitation, leading to an optimized LSTM model with improved predictive performance. The optimal configuration identified comprised a single recurrent layer with 43 hidden units, a learning rate of approximately 1.48×10^{-5}, and a batch size of 21. The LSTM model was trained for 1000 epochs, incorporating early stopping to mitigate overfitting. Model performance was assessed using the root mean square error (RMSE) metric. The training and testing set RMSE values were found to be 1.88e-04 and 7.63e-04, respectively, indicating effective model training. To further investigate model performance, RMSE values were computed for all time steps corresponding to each wind direction and at specific time steps (1000th, 5000th, and 8000th, each representing 0.001 s). The results of these evaluations for the unconstrained scenario are summarized in Table 1. As the proposed model predicts the time history of wind pressure coefficients, the presented RMSE values are therefore dimensionless.

The results demonstrate consistently low RMSE values across all wind directions for both the training and testing sets. To provide further insight, RMSE was calculated in two ways: across the entire temporal and spatial domain (labeled "Total RMSE" in Table 1) and at randomly selected time steps across all points on the building façade (labeled "RMSE" in Table 1). For instance, the overall training set RMSE does not exceed 0.0159 (observed at 5°), with lower values obtained at 30° (0.0121). Similarly, the testing set exhibits low RMSE values, reaching 0.0328 at 45°, compared to 0.0144 at 20°. Analogous trends are observed for other wind directions within both sets. Furthermore, the consistently low RMSE values across different time steps (1000th, 5000th, and 8000th) indicate the effectiveness of the LSTM model in predicting time series wind pressure.

TABLE 1 Root mean square error (RMSE) values for predicting wind pressure coefficients (windward case).

	Wind direction	Time step	RMSE	Total RMSE
Training set	5°	1000	0.0115	0.0159
		5000	0.0164	
		8000	0.0185	
	30°	1000	0.0091	0.0121
		5000	0.0154	
		8000	0.0112	
	50°	1000	0.1389	0.0134
		5000	0.0118	
		8000	0.0221	
Test set	0°	1000	0.0173	0.0193
		5000	0.0237	
		8000	0.0185	
	20°	1000	0.0084	0.0144
		5000	0.0162	
		8000	0.1780	
	45°	1000	0.0322	0.0328
		5000	0.0363	
		8000	0.0223	

3.4 | Application and results

This section presents a comprehensive evaluation of the proposed framework's performance across the four sensor placement scenarios: the unconstrained scenario (Scenario 1), the predefined sensors scenario (Scenario 2), the region-constrained scenario (Scenario 3), and the limited-number-of-sensors scenario (Scenario 4). Each scenario is examined under three distinct wind directions to assess the framework's ability to generalize across varying wind conditions. The accuracy of the proposed framework is evaluated at two different time steps for each scenario. The model performance is assessed by comparing the predicted results with true pressure data, utilizing both visual inspection and quantitative analysis using the RMSE metric. The results of this comparative analysis for the windward façade are visualized in Figure 3.

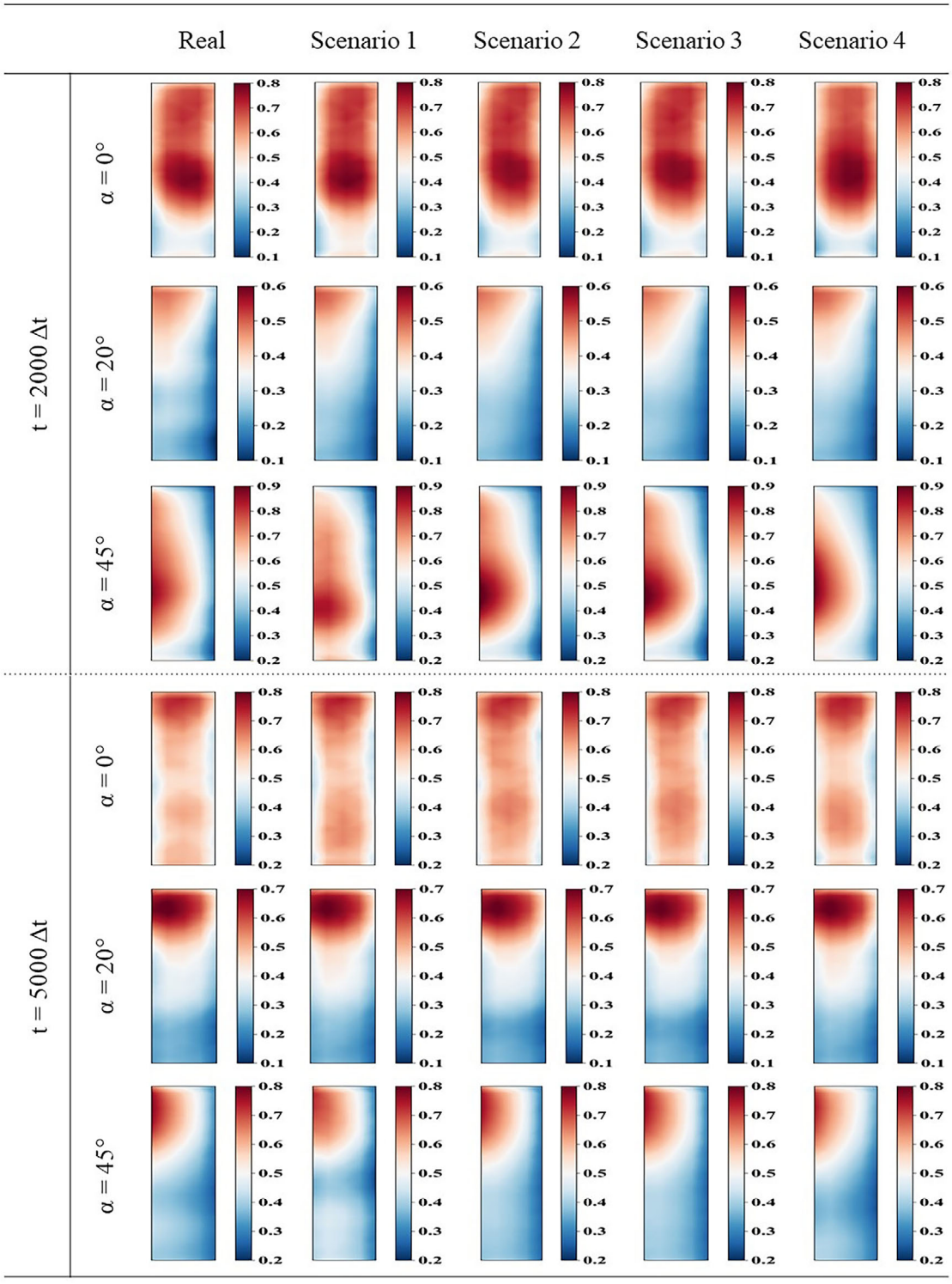

FIGURE 3 Predicted wind pressure distributions at two-time steps for different wind directions and sensor constraints (windward).

Figure 3 demonstrates the capability of the proposed model to generate accurate pressure distributions across all scenarios, including both unconstrained and constrained sensor placements. This consistency is observed not only for the wind direction of 0°, for which the sensor placement was optimized for the windward façade but also for other directions where sensor placement may be less ideal. Notably, even in the most challenging scenario (Scenario 4), which involves the use of only five sensors, the model demonstrated the ability to produce accurate simulation results. Quantitative analysis further supports these observations. For the windward façade, at the 0°

wind direction, RMSE values at time step 2000 are 0.0224, 0.0220, 0.0158, and 0.0132, respectively, for scenarios 1–4. At time step 5000, these values are 0.0234, 0.0302, 0.0226, and 0.0237. The low RMSE values obtained for different scenarios demonstrate the capability of the proposed framework in reconstructing wind pressures considering various constraints. Similar trends are observed for other wind directions. For the windward façade, at the 20° wind direction, RMSE values at time step 2000 are 0.0135, 0.0107, 0.0184, and 0.0297, and at time step 5000 are 0.0144, 0.0106, 0.0175, and 0.0171. Likewise, for the windward façade, at the 45° wind direction, RMSE values at time step 2000 are 0.0471, 0.0102, 0.0340, and 0.0165, and at time Step 5000 are 0.0289, 0.0159, 0.0264, and 0.0381. These results consistently demonstrate the model's ability to generalize and provide accurate predictions across a range of wind conditions.

Despite the complex aerodynamic effects of wake turbulence and vortex shedding on the right-side and leeward façades (illustrated in Figure 4), the model maintains strong predictive performance, which was further evaluated by selecting different time steps for visualization and comparison. The LSTM model successfully learned to map the low-fidelity pressure field (reconstructed using 25 unconstrained sensors) to the high-fidelity field. For the right-side façade, total RMSE values of 0.1640, 0.0293, and 0.0794 were obtained for wind directions of 10°, 20°, and 40°, respectively. While higher than the windward case, the reconstructed high-fidelity distributions still closely match the real data. The leeward façade exhibited even better predictive accuracy, as shown in Figure 4, with significantly lower total RMSE values of 0.0336, 0.0248, and 0.0264 for the same wind directions. This demonstrates the model's ability to generalize effectively to complex wind interactions beyond simple windward conditions.

The model's ability to capture the temporal evolution of wind pressure is demonstrated by the time histories of the pressure coefficients at several key locations. Figure 5 shows the results for four representative points on the leeward façade ($\alpha = 10°$) and two on the right face ($\alpha = 20°$) for Scenario 1. Notably, Sensors 2 and 3 on the leeward side, and Sensor 6 on the right side, achieve the highest accuracy, with RMSE values of 0.0129, 0.0204, and 0.0173, respectively. In contrast, the corner sensors exhibit the highest RMSE values of 0.0549, 0.1481, and 0.1391 for Sensors 1, 4, and 5. Comparable results are also observed at other sensor locations, further underscoring the model's robust performance. Despite these variations, all RMSE values remain below 0.15, indicating strong agreement between the predicted and true pressure coefficients and emphasizing the model's precision in capturing the dynamic fluctuations of the wind pressure field.

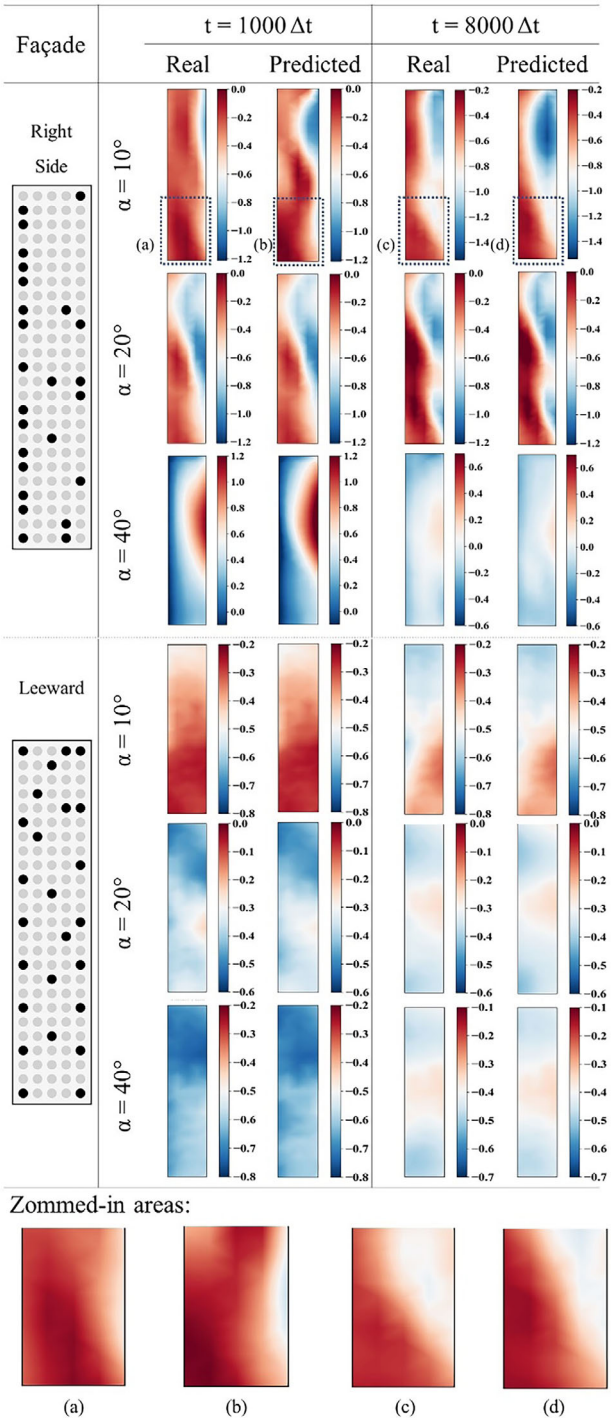

FIGURE 4 Predicted wind pressure distributions for right-side and leeward façades with sensor locations indicated.

Finally, to demonstrate the effectiveness of the proposed POD-LSTM framework, a comparative analysis is conducted against two alternative approaches:

1. LSTM without POD: A model trained directly on the original high-dimensional sensor data, without prior dynamic feature extraction.

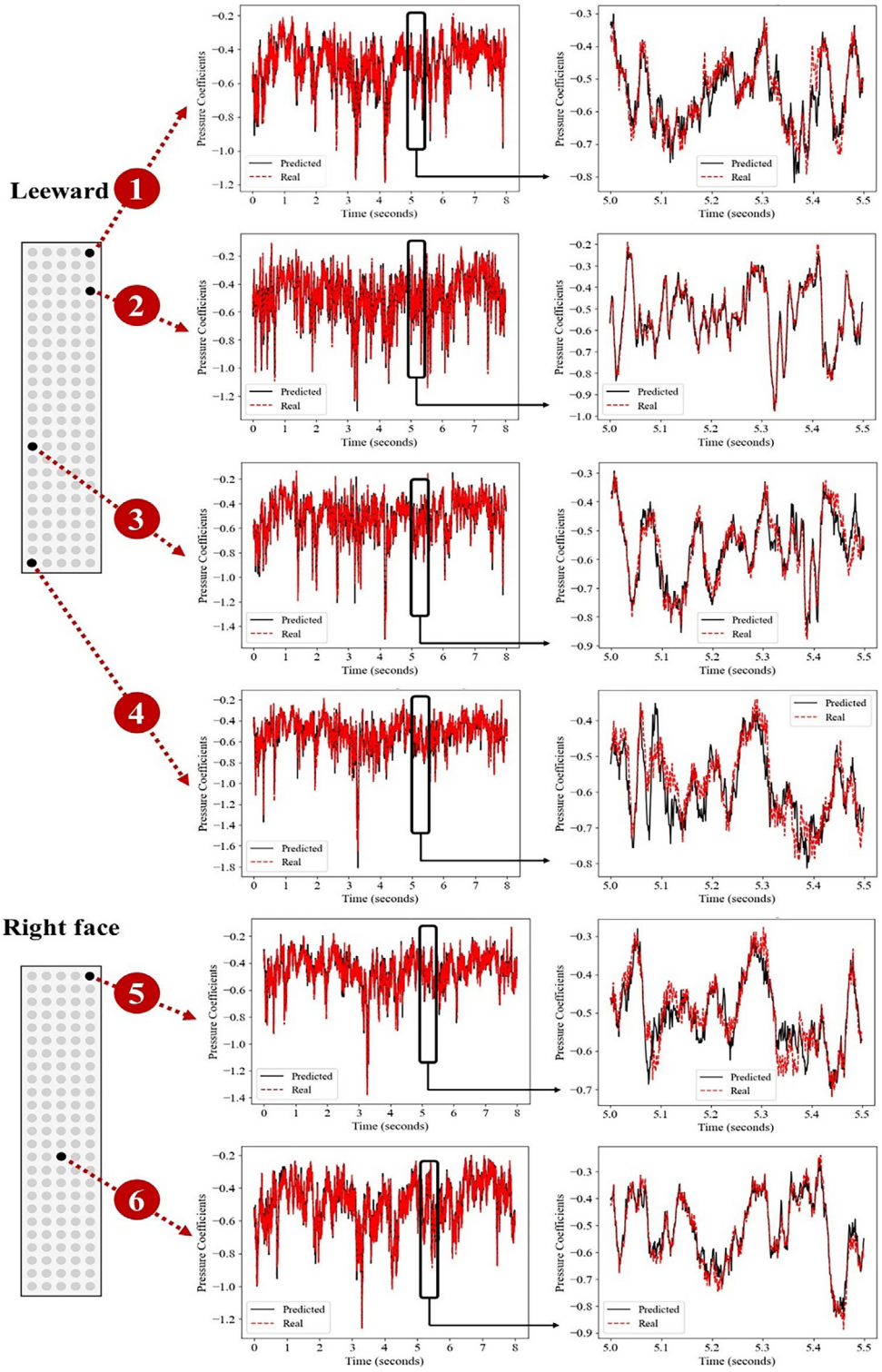

FIGURE 5 Time history comparison of predicted and actual pressure coefficients for four sensors on the leeward façade ($\alpha = 10°$) and two sensors on the right façade ($\alpha = 20°$) in Scenario 1.

2. ANN mapping: A fully connected network that directly maps sparse sensor inputs to the full pressure field, similar to the approach used by Erichson et al. (2020) who employed shallow neural networks for vorticity field reconstruction from limited sensors in fluid flow, demonstrating the potential of ANNs for flow field approximation.

This comparison is performed for the windward façade. The results of this comparison, presented in Figure 6,

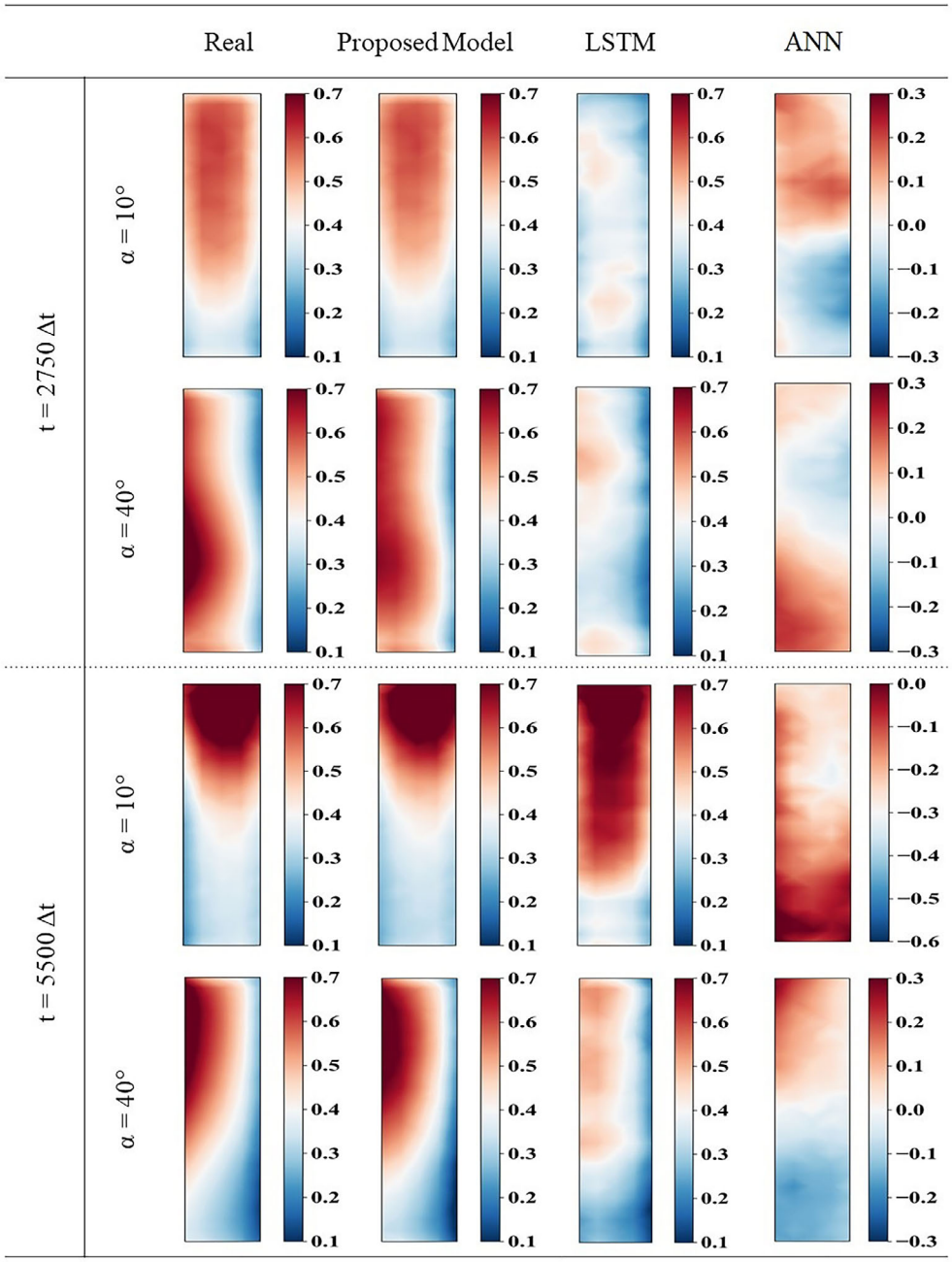

FIGURE 6 Performance comparison of the proposed hybrid model against LSTM and ANN.

demonstrate that the proposed POD-LSTM framework outperforms both the LSTM without POD and the ANN mapping, achieving higher accuracy and demonstrating the benefits of dimensionality reduction and dynamic feature extraction. Similar results are obtained for the other façades. It should be noted that according to Figure 6, the ANN model performs slightly better than the LSTM model because a separate ANN model is trained for each wind direction due to the complexity of the pressure distribution and the ANN's limited ability to generalize across different wind directions. In contrast, a single LSTM network was trained for all wind directions.

In summary, the results across all façades demonstrate the effectiveness of the proposed POD-LSTM framework in accurately reconstructing wind pressure distributions, even in complex scenarios and with constrained sensor configurations. Specifically, even for the right-side and leeward façades, where the flow fields are more complex due to wake effects and vortex shedding, the model consistently achieves low RMSE values, indicating its ability to generalize and provide reliable predictions under challenging conditions. This highlights the potential of the framework for real-world applications in structural health monitoring and digital twin development, where accurate pressure

field reconstruction is crucial for ensuring the safety and serviceability of high-rise buildings.

4 | DISCUSSION

The current study demonstrates the potential of the proposed hybrid POD-LSTM model in predicting wind pressure coefficient distributions across building façades using a limited number of sensors. By leveraging a reduced sensor configuration, the model accurately estimates wind pressure for various wind directions, showcasing its capability in practical applications where sensor placement may be constrained due to budgetary, structural, or aesthetic factors. Three different constraining scenarios—including predefined sensor locations, restricted regions, and a scenario with an extremely limited number of sensors—were thoroughly evaluated, confirming the model's robustness under these conditions.

Unlike conventional sensor-based interpolation or direct ML-based reconstructions, the proposed approach maps the dynamic features of the wind pressure field from low-fidelity to high-fidelity representations. Even when the sensor placement was optimized for only one wind direction, the model generalizes well to other wind directions, demonstrating its ability to handle different flow conditions. This is attributed to the dynamic mapping approach (Conti et al., 2024), which transforms low-fidelity pressure reconstructions obtained from a highly constrained sensor setup into an enhanced high-fidelity representation. Additionally, accurate predictions are achieved not only on the windward façade but also on the right-side and leeward façades, which are more aerodynamically complex due to wake turbulence and vortex shedding.

Despite the promising results, several limitations should be acknowledged. A key assumption is the availability of high-fidelity data, in this case, obtained from wind tunnel experiments. While CFD simulations could also serve as a data source, significant changes in the surrounding environment (e.g., construction of new buildings) would inevitably alter local wind conditions and affect the existing POD modes. Reanalysis would be necessary to capture the updated system dynamics. Furthermore, although POD effectively extracts dominant flow features, multiresolution DMD, wavelet decompositions, or autoencoders could be explored to handle nonstationary flow dynamics and improve robustness in varying environmental conditions. To further improve the model's generalization ability, especially when labeled training data are scarce, exploring alternative spatiotemporal ML models like self-supervised learning techniques (Rafiei et al., 2024a, 2024b) could be beneficial. Additionally, hybrid ML approaches, including customized kernel support vector regression and probabilistic neural networks optimized using metaheuristic algorithms like those employing particle swarm optimization (Hossain et al., 2019) and spider monkey optimization (Akhand et al., 2020), as well as other methods (Wang et al., 2018), could be investigated to enhance predictive accuracy under complex conditions. On the other hand, the proposed model assumes a fixed number of functional sensors based on predefined configurations. However, in real-world applications, sensor failures or malfunctions are inevitable, leading to incomplete or missing data (Kim et al., 2022). Since the proposed model is trained on a specific sensor arrangement, its performance may degrade if sensor data become unavailable. To mitigate this issue, additional training with various sensor failure scenarios might be necessary to improve the model's adaptability and reliability under such conditions. Moreover, while the proposed methodology successfully predicts wind pressure distributions for varying wind directions within the given conditions, generalization to different environmental conditions, exposure, and building geometry may require additional training data; however, the same proposed approach remains applicable to different configurations, and techniques like transfer learning (Azimi & Yang, 2024) might assist in adapting to these new configurations. Furthermore, even with extensive sensor coverage, accurately capturing highly localized pressure features, particularly at geometric extremities, can present a challenge. Additionally, the framework's reliance on relative pressure sensor data might necessitate additional calibration and preprocessing steps for direct application with absolute pressure sensors. While utilizing the normalized pressure coefficients can reduce sensor-specific biases, adapting the methodology for use with absolute sensors (e.g., Hochschild & Gorlé, 2024a, 2024b) would likely require further validation and adjustments.

Overall, the results confirm that the hybrid POD-LSTM framework provides a robust and computationally efficient solution for wind pressure coefficient reconstruction under sensor constraints. By addressing the identified limitations, the methodology can be further enhanced for structural health monitoring, digital twin applications, and real-time wind pressure estimation in urban environments.

5 | CONCLUSION

This study presented a novel hybrid ML framework for reconstructing HFWP coefficient fields from a limited number of sensors, addressing challenges in sensor deployment due to cost, accessibility, and structural constraints. The proposed approach integrates constrained

sensor placement and wind pressure reconstruction, POD for dynamic feature extraction, and LSTM networks for time-dependent mapping, enabling accurate wind pressure estimations with minimal sensor coverage. The effectiveness of the framework is demonstrated through case studies using wind tunnel data from TPU, where multiple sensor placement constraints were considered.

The results confirm that the model accurately reconstructs wind pressure coefficient distributions across multiple façades—including the windward, right-side, and leeward façades—even under extreme sensor limitations. Notably, the model generalizes well to unseen wind directions, highlighting its ability to adapt to varying flow conditions. For example, in the unconstrained sensor scenario, the overall training set RMSE for the windward case remains below 0.0159, and the testing set exhibits similarly low RMSE values, reaching up to 0.0328. Even in the challenging scenario with only five sensors, the RMSE values are around 0.03. For the more complex right-side and leeward façades, which are affected by wake turbulence and vortex shedding, the model maintains strong predictive performance with expectedly higher RMSE values (around 0.04 for the leeward side), still achieving a generally good reconstruction of the full pressure field. A comparative evaluation with alternative ML approaches further demonstrates the superiority of the proposed method. The hybrid POD-LSTM framework outperforms direct ANN-based mapping and LSTM models trained without dynamic feature extraction, achieving higher accuracy while maintaining computational efficiency. These results confirm the importance of dynamic feature extraction and reduced-order modeling in enhancing wind pressure field reconstruction. These findings suggest significant potential for practical applications in structural monitoring and building design, where sensor deployment may be constrained by cost, accessibility, or architectural limitations. By enabling accurate pressure estimations with minimal sensor requirements, this framework provides a valuable tool for enhancing the safety and resilience of structures in urban environments.

ACKNOWLEDGMENTS

This work was supported by the Natural Sciences and Engineering Research Council of Canada (NSERC) [Grant Number CRSNG RGPIN 2022-03492].

REFERENCES

Aboshosha, H., Elshaer, A., Bitsuamlak, G. T., & El Damatty, A. (2015). Consistent inflow turbulence generator for LES evaluation of wind-induced responses for tall buildings. *Journal of Wind Engineering and Industrial Aerodynamics*, *142*, 198–216.

Ahmadi, J., Mahdavinejad, M., Larsen, O. K., Zhang, C., Zarkesh, A., & Asadi, S. (2022). Evaluating the different boundary conditions to simulate airflow and heat transfer in Double-Skin Facade. *Building Simulation*, *15*, 799–815.

Akhand, M. A. H., Ayon, S. I., Shahriyar, S. A., Siddique, N., & Adeli, H. (2020). Discrete spider monkey optimization for travelling salesman problem. *Applied Soft Computing*, *86*, 105887.

Al Sayegh, H., Chowdhury, A. G., Zisis, I., Elawady, A., Estephan, J., & Tolera, A. (2025). Full-scale experimental investigation of wind loading on ballasted photovoltaic arrays mounted on flat roofs. *Journal of Wind Engineering and Industrial Aerodynamics*, *256*, 105963.

Amezquita-Sanchez, J. P., Valtierra-Rodriguez, M., & Adeli, H. (2018). Wireless smart sensors for monitoring the health condition of civil infrastructure. *Scientia Iranica*, *25*(6), 2913–2925.

Amini, M., & Memari, A. M. (2021). CFD-based evaluation of elevated coastal residential buildings under hurricane wind loads. *Journal of Architectural Engineering*, *27*(3), 04021014.

Arbelo Romero, J. M., Blocken, B., Hemida, H., & Sterling, M. (2024). *On the performance of SRANS, URANS and SAS in the prediction of the wind characteristics around a high-rise building*. https://doi.org/10.2139/ssrn.4918297

Avini, R., Kumar, P., & Hughes, S. J. (2019). Wind loading on high-rise buildings and the comfort effects on the occupants. *Sustainable Cities and Society*, *45*, 378–394.

Azimi, M., & Yang, T. Y. (2024). Transformer-based framework for accurate segmentation of high-resolution images in structural health monitoring. *Computer-Aided Civil and Infrastructure Engineering*, *39*(24), 3670–3684.

Bre, F., & Gimenez, J. M. (2022). A cloud-based platform to predict wind pressure coefficients on buildings. *Building Simulation*, *15*(8), 1507–1525.

Bre, F., Gimenez, J. M., & Fachinotti, V. D. (2018). Prediction of wind pressure coefficients on building surfaces using artificial neural networks. *Energy and Buildings*, *158*, 1429–1441.

Clemente, A. V., Giljarhus, K. E. T., Oggiano, L., & Ruocco, M. (2024). Rapid pedestrian-level wind field prediction for early-stage design using Pareto-optimized convolutional neural networks. *Computer-Aided Civil and Infrastructure Engineering*, *39*(18), 2826–2839.

Cid Montoya, M., Mishra, A., Verma, S., Mures, O. A., & Rubio-Medrano, C. E. (2024). Aeroelastic force prediction via temporal fusion transformers. *Computer-Aided Civil and Infrastructure Engineering*, Advance online publication. https://doi.org/10.1111/mice.13381

Conti, P., Guo, M., Manzoni, A., Frangi, A., Brunton, S. L., & Nathan Kutz, J. (2024). Multi-fidelity reduced-order surrogate modelling. *Proceedings of the Royal Society A: Mathematical, Physical and Engineering Sciences*, *480*, 2283. https://doi.org/10.1098/rspa.2023.0655

Dogan, T., & Kastner, P. (2021). Streamlined CFD simulation framework to generate wind-pressure coefficients on building facades for airflow network simulations. *Building Simulation*, *14*, 1189–1200.

Entezami, A., & Sarmadi, H. (2024). Machine learning-aided prediction of windstorm-induced vibration responses of long-span suspension bridges. *Computer-Aided Civil and Infrastructure Engineering*, Advance online publication. https://doi.org/10.1111/mice.13387

Erichson, N. B., Mathelin, L., Yao, Z., Brunton, S. L., Mahoney, M. W., & Kutz, J. N. (2020). Shallow neural networks for fluid flow reconstruction with limited sensors. *Proceedings of the Royal Society A*, *476*(2238), 20200097.

Fernández-Cabán, P. L., Masters, F. J., & Phillips, B. M. (2018). Predicting roof pressures on a low-rise structure from freestream turbulence using artificial neural networks. *Frontiers in Built Environment*, *4*, 68.

Gao, H., Hu, G., Zhang, D., Jiang, W., Tse, K. T., Kwok, K. C. S., & Kareem, A. (2024). Urban wind field prediction based on sparse sensors and physics-informed graph-assisted autoencoder. *Computer-Aided Civil and Infrastructure Engineering*, *39*(10), 1409–1430.

Gao, H., Liu, J., Lin, P., Hu, G., Patruno, L., Xiao, Y., & Kwok, K. C. S. (2023). An optimal sensor placement scheme for wind flow and pressure field monitoring. *Building and Environment*, *244*, 110803.

Gu, D. L., Shuai, Q. W., Zhang, N., Jin, N., Zheng, Z. X., Xu, Z., & Xu, Y. J. (2025). Multi-view street view image fusion for city-scale assessment of wind damage to building clusters. *Computer-Aided Civil and Infrastructure Engineering*, *40*(2), 198–214.

Gutierrez Soto, M., & Adeli, H. (2013). Placement of control devices for passive, semi-active, and active vibration control of structures. *Scientia Iranica*, *20*(6), 1567–1578.

Han, X. L., Li, Q. S., Zhou, K., & Li, X. (2022). Comparative study between field measurements of wind pressures on a 600-m-high skyscraper during Super Typhoon Mangkhut and wind tunnel test. *Engineering Structures*, *272*, 114958.

Hochschild, J., & Gorlé, C. (2024a). Design and demonstration of a sensing network for full-scale wind pressure measurements on buildings. *Journal of Wind Engineering and Industrial Aerodynamics*, *250*, 105760.

Hochschild, J., & Gorlé, C. (2024b). Comparison of measured and LES-predicted wind pressures on the Space Needle. *Journal of Wind Engineering and Industrial Aerodynamics*, *249*, 105749.

Hou, F., & Jafari, M. (2020). Investigation approaches to quantify wind-induced load and response of tall buildings: A review. *Sustainable Cities and Society*, *62*, 102376.

Hossain, S. I., Akhand, M. A. H., Shuvo, M. I. R., Siddique, N., & Adeli, H. (2019). Optimization of university course scheduling problem using particle swarm optimization with selective search. *Expert systems with Applications*, *127*, 9–24.

Hu, G., & Kwok, K. C. (2020). Predicting wind pressures around circular cylinders using machine learning techniques. *Journal of Wind Engineering and Industrial Aerodynamics*, *198*, 104099.

Hu, G., Liu, L., Tao, D., Song, J., & Kwok, K. C. S. (2019). *Investigation of wind pressures on tall building under interference effects using machine learning techniques*. arXiv preprint arXiv:1908.07307. https://doi.org/10.48550/arXiv.1908.07307

Huang, J. X., Li, Q. S., & Han, X. L. (2022). Recovery of missing field measured wind pressures on a supertall building based on correlation analysis and machine learning. *Journal of Wind Engineering and Industrial Aerodynamics*, *231*, 105237.

Inoue, T., Ikami, T., Egami, Y., Nagai, H., Naganuma, Y., Kimura, K., & Matsuda, Y. (2023). Data-driven optimal sensor placement for high-dimensional system using annealing machine. *Mechanical Systems and Signal Processing*, *188*, 109957.

Inoba, R., Uchida, K., Iwasaki, Y., Nagata, T., Ozawa, Y., Saito, Y., Nonomura, T., & Asai, K. (2022). Optimization of sparse sensor placement for estimation of wind direction and surface pressure distribution using time-averaged pressure-sensitive paint data on automobile model. *Journal of Wind Engineering and Industrial Aerodynamics*, *227*, 105043.

Karnik, N., Abdo, M. G., Estrada-Perez, C. E., Yoo, J. S., Cogliati, J. J., Skifton, R. S., Calderoni, P., Brunton, S. L., & Manohar, K. (2024). Constrained optimization of sensor placement for nuclear digital twins. *IEEE Sensors Journal*, *24*(9), 15501–15516.

Kim, S., Kim, H. K., & Spencer, B. F. (2022). Automated damping identification of long-span bridge using long-term wireless monitoring data with multiple sensor faults. *Journal of Civil Structural Health Monitoring*, *12*(2), 465–479.

Kim, B., Yuvaraj, N., Tse, K. T., Lee, D. E., & Hu, G. (2021). Pressure pattern recognition in buildings using an unsupervised machine-learning algorithm. *Journal of Wind Engineering and Industrial Aerodynamics*, *214*, 104629.

Kim, H., & Adeli, H. (2005). Wind-induced motion control of 76-story benchmark building using the hybrid damper-TLCD system. *Journal of Structural Engineering*, *131*(12), 1794–1802.

Kociecki, M., & Adeli, H. (2014). Two-phase genetic algorithm for topology optimization of free-form steel space-frame roof structures with complex curvatures. *Engineering Applications of Artificial Intelligence*, *32*, 218–227.

Lamberti, G., & Gorlé, C. (2021). A multi-fidelity machine learning framework to predict wind loads on buildings. *Journal of Wind Engineering and Industrial Aerodynamics*, *214*, 104647.

Li, S., Snaiki, R., & Wu, T. (2021a). A knowledge-enhanced deep reinforcement learning-based shape optimizer for aerodynamic mitigation of wind-sensitive structures. *Computer-Aided Civil and Infrastructure Engineering*, *36*(6), 733–746.

Li, S., Snaiki, R., & Wu, T. (2021b). Active simulation of transient wind field in a multiple-fan wind tunnel via deep reinforcement learning. *Journal of Engineering Mechanics*, *147*(9), 04021056.

Li, Y., Yin, P. K., & Chen, F. B. (2024). Prediction of wind load power spectrum on high-rise buildings by various machine learning algorithms. *Structures*, *67*, 107015.

Li, Y., Huang, X., Li, Y. G., Chen, F. B., & Li, Q. S. (2022). Machine learning based algorithms for wind pressure prediction of high-rise buildings. *Advances in Structural Engineering*, *25*(10), 2222–2233.

Liang, Q. S., Fu, J. Y., Li, Z., Yan, B. W., Shu, Z. R., & He, Y. C. (2020). Bimodal distribution of wind pressure on windward facades of high-rise buildings induced by interference effects. *Journal of Wind Engineering and Industrial Aerodynamics*, *200*, 104156.

Luo, X., & Kareem, A. (2021). Dynamic mode decomposition of random pressure fields over bluff bodies. *Journal of Engineering Mechanics*, *147*(4), 04021007.

Luo, X., Kareem, A., & Yoo, S. (2023). Optimal sensor placement for reconstructing wind pressure field around buildings using compressed sensing. *Journal of Building Engineering*, *75*, 106855.

McGuill, C., & Keenahan, J. (2020). A parametric study of wind pressure distribution on façades using computational fluid dynamics. *Applied Sciences*, *10*(23), 8627.

Meddage, D. P. P., Mohotti, D., & Wijesooriya, K. (2024). Predicting transient wind loads on tall buildings in three-dimensional spatial coordinates using machine learning. *Journal of Building Engineering*, *85*, 108725.

Meddage, D. P. P., Mohotti, D., Wijesooriya, K., Lee, C. K., & Kwok, K. C. S. (2025). Interpolating wind pressure time-histories around

a tall building—A deep learning-based approach. *Journal of Wind Engineering and Industrial Aerodynamics*, *256*, 105968.

Meng, F. Q., He, B. J., Zhu, J., Zhao, D. X., Darko, A., & Zhao, Z. Q. (2018). Sensitivity analysis of wind pressure coefficients on CAARC standard tall buildings in CFD simulations. *Journal of Building Engineering*, *16*, 146–158.

Montazeri, H., & Blocken, B. (2013). CFD simulation of wind-induced pressure coefficients on buildings with and without balconies: Validation and sensitivity analysis. *Building and Environment*, *60*, 137–149.

Naeini, S. S., & Snaiki, R. (2024). A novel hybrid machine learning model for rapid assessment of wave and storm surge responses over an extended coastal region. *Coastal Engineering*, *190*, 104503.

Nav, F. M., & Snaiki, R. (2025). Time-domain buffeting response prediction of a long-span bridge: A hybrid machine learning framework. *Structures*, *73*, 108286.

Oh, B. K., Glisic, B., Kim, Y., & Park, H. S. (2019). Convolutional neural network-based wind-induced response estimation model for tall buildings. *Computer-Aided Civil and Infrastructure Engineering*, *34*(10), 843–858.

Pezeshki, H., Pavlou, D., Adeli, H., & Siriwardane, S. (2024). Gyroscopic effects of the spinning rotor-blades assembly on dynamic response of offshore wind turbines. *Journal of Wind Engineering and Industrial Aerodynamics*, *247*, 105698.

Pezeshki, H., Pavlou, D., Adeli, H., & Siriwardane, S. C. (2023). Modal analysis of offshore monopile wind turbine: An analytical solution. *Journal of Offshore Mechanics and Arctic Engineering*, *145*(1), 010907.

Rafiei, M. H., Gauthier, L. V., Adeli, H., & Takabi, D. (2024a). Self-supervised learning for electroencephalography. *IEEE Transactions on Neural Networks and Learning Systems*, *35*(2), 1457–1471.

Rafiei, M. H., Gauthier, L. V., Adeli, H., & Takabi, D. (2024b). Self-supervised learning for near-wild cognitive workload estimation. *Journal of Medical Systems*, *48*(1), 107.

Sharma, A., Mittal, H., & Gairola, A. (2018). Mitigation of wind load on tall buildings through aerodynamic modifications. *Journal of Building Engineering*, *18*, 180–194.

Snaiki, R., & Mirfakhar, S. F. (2024). Multiresolution dynamic mode decomposition approach for wind pressure analysis and reconstruction around buildings. *Computer-Aided Civil and Infrastructure Engineering*, *39*(22), 3375–3391.

Tominaga, Y., Wang, L. L., Zhai, Z. J., & Stathopoulos, T. (2023). Accuracy of CFD simulations in urban aerodynamics and microclimate: Progress and challenges. *Building and Environment*, *243*, 110723.

Wang, N., & Adeli, H. (2015). Robust vibration control of wind-excited highrise building structures. *Journal of Civil Engineering and Management*, *21*(8), 967–976.

Wang, H., Ma, W., Niu, J., & You, R. (2025). Evaluating a deep learning-based surrogate model for predicting wind distribution in urban microclimate design. *Building and Environment*, *269*, 112426.

Wang, J., Zhong, D., Adeli, H., Wang, D., & Liu, M. (2018). Smart bacteria-foraging algorithm-based customized kernel support vector regression and enhanced probabilistic neural network for compaction quality assessment and control of earth-rock dam. *Expert Systems*, *35*(6), e12357.

Wei, J., Shen, T., Wang, K., Liu, J., Wang, S., & Hu, W. (2025). Transfer learning framework for the wind pressure prediction of high-rise building surfaces using wind tunnel experiments and machine learning. *Building and Environment*, *271*, 112620.

Weng, Y., & Paal, S. G. (2022). Machine learning-based wind pressure prediction of low-rise non-isolated buildings. *Engineering Structures*, *258*, 114148.

Whiteman, M. L., Fernández-Cabán, P. L., Phillips, B. M., Masters, F. J., Davis, J. R., & Bridge, J. A. (2022). Cyber-physical aerodynamic shape optimization of a tall building in a wind tunnel using an active fin system. *Journal of Wind Engineering and Industrial Aerodynamics*, *220*, 104835.

Wu, T., & Snaiki, R. (2022). Applications of machine learning to wind engineering. *Frontiers in Built Environment*, *8*, 811460.

Yao, H., Tan, P., Yang, T. Y., & Zhou, F. (2024). Deep reinforcement learning-based active mass driver decoupled control framework considering control–structure interaction effects. *Computer-Aided Civil and Infrastructure Engineering*, *39*(11), 1573–1596.

Zhao, L., Zhang, L., Cui, W., Cao, S., & Ge, Y. (2024). The reproduction of 2-D non-synoptic wind field in an actively controlled wind tunnel. *Journal of Wind Engineering and Industrial Aerodynamics*, *251*, 105786.

How to cite this article: Nav, F. M., Mirfakhar, S. F., & Snaiki, R. (2025). A hybrid machine learning framework for wind pressure prediction on buildings with constrained sensor networks. *Computer-Aided Civil and Infrastructure Engineering*, 1–17. https://doi.org/10.1111/mice.13488